Research on sound field characteristics of full-ceramic angular contact ball bearing

Haipeng Yan[1,2,3] · Yuhou Wu[1,2] · Songhua Li[1,2] · Lixiu Zhang[1,2] · Ke Zhang[1,2]

Abstract
This paper focuses on the distribution characteristics of the radiation noise for a full-ceramic angular contact ball bearing (FCACBB). A model for calculating the radiation noise of a FCACBB was established based on the bearing dynamic characteristics and sound radiation theory, and the effectiveness and accuracy of the method were verified by corresponding experiments. The variation of the radiation noise for a FCACBB with the rotational speed was analyzed. The directivity of the sound field in the circumferential direction was found. The variation trends of the radiation noise in the friction load zone and the impact load zone were discussed. The attenuation of the radiation noise in the radial direction and in the axial direction was investigated. The directivity angle and the degree of directivity of the sound field were explored at different radial and axial distances. The results show that the inhomogeneous contacts between the bearing components in the circumferential direction result in different degrees of friction and impact vibration at different locations, which makes the radiation noise of the FCACBB have a larger component in the radial direction than in the axial direction. The conclusions can provide a reference for predicting the radiation noise of FCACBBs and further optimizing the sound field.

1 Introduction

Angular contact bearings are widely used in high-speed applications, which can withstand large unidirectional axial loads. However, with the progress of science and technology, greenness, intellectualization and high reliability has become the goal of customers and is also the development trend of bearings. Bearing plays an important role in the equipment. The failure of bearings during the working will affect the accuracy of mechanical system, and even more serious consequences will occur [1]. Compared with steel bearings, ceramic bearings have better wear resistance and higher thermal stability [2, 3], so their operation accuracy and reliability are also higher, bringing to a wide application in the fields of high technology. About the performance analysis of high-speed angular contact ball bearings, currently, there are five types of dynamic analytical models for rolling bearings, namely the lumped-parameter, quasi-static, quasi-dynamic, dynamic, and finite element models [4]. Nowadays, many scholars have studied the effects of preload [5], stiffness [6], contact angle [7], raceway surface roughness [8], and waviness [9] on the dynamic characteristics of the bearing in particular, as well as skidding behavior [10, 11]. Zhang et al. [12] researched the impact of lubricant traction coefficient on cage's dynamic characteristics in high-speed angular contact bearing, and the stability of cage under various working conditions was assessed by the slip ratio of cage. Jiang et al. [13–15] researched the variable optimum preload of the bearing utilizing the transfer matrix method and systematically discussed the dynamic characteristics of bearings. In addition, some researchers discussed the thermal characteristics of bearings, lubrication and air supply method [16–20] as well as the dynamic response with fault conditions [21–24]. However, the acoustic performance of

✉ Yuhou Wu
sjzuwuyh@163.com

1 School of Mechanical Engineering, Shenyang Jianzhu University, Shenyang 110168, China

2 National-Local Joint Engineering Laboratory of NC Machining Equipment and Technology of High-Grade Stone, Shenyang 110168, China

3 School of Mechanical Engineering, Hebei University of Science and Technology, Shijiazhang 050018, China

bearings is rarely reported [25, 26], and the structures and properties of ceramic bearings are few studies [27–29].

Bearing noise is mainly generated by the interaction between the components of the bearing and is closely related to the material, structural parameters, contact surface, lubrication, and working conditions of the bearing [30–32]. For a full-ceramic angular contact ball bearing (FCACBB), hardness and brittleness itself leads to great noise in the operation, which is different from the steel bearings. On the one hand, the great sound radiation limits the application of full-ceramic bearings for military or other equipment with demand of quietness, and on the other hand, bearing noise is an important indicator of bearing performance, which reflects the quality of bearing to some extent. Moreover, the sound pollution also brings serious physical and mental health effects to workers. Bearing noise is the primary sound source of machinery equipment. Reducing bearing noise can not only make sure that the operators work in a green environment, but also improve the bearing performance. However, the varied decibels of sound may be heard in the bearing sound field at different locations away from the sound source. Accordingly, the prediction and analysis of the sound field characteristics of the FCACBBs are quite essential for the reduction of noise and optimization of sound field.

To investigate the radiation noise characteristics of FCACBBs and the distribution characteristics of the sound field, the dynamic model of a FCACBB is presented considering oil film force and gravity of the ceramic ball, and then combining the dynamic model and the sound radiation theory, the model of the bearing radiation noise is established. The distribution function of sound pressure level at different field points is further analyzed. The variation of the radiation noise with the working speed of the bearing and the distribution characteristics of the sound field in the circumferential, radial, and axial directions is studied.

## 2 Sound radiation characteristics of full-ceramic bearing

As is known to all, a ball bearing consists of four components such as balls, cage, inner and outer rings. Generally, in actual operations, the outer ring of the bearing is assembled into the bearing pedestal, and it is considered fixed. The inner ring rotates at a constant speed. Here, the radiation noise model of a FCACBB is established based on the dynamic characteristics of bearings and acoustic theory. A number of indicators are used to characterize the sound field characteristics, and then, the calculation of the radiation noise is conducted.

2.1 Calculated model on sound radiation

Assuming that the center of mass of each bearing component is consistent with the geometrical center, the movement of the cage is guided by the inner ring. To better analyze the vibration and noise characteristics of the high-speed FCACBB, as shown in Fig. 1, the interactions among the bearing components are first analyzed. Then, the differential equations of vibration for each bearing component are established. The radiation sound pressure of a FCACBB is further calculated.

In Fig. 1, the inertial coordinate system $\{O; X, Y, Z\}$ is fixed, and coordinate origin O is fixed to the initial center of the bearing. The X-axis represents the bearing rotation axis, which is parallel to the ground. The Y and Z axes represent the horizontal radial and vertical radial directions, respectively. The following notation is used to describe the components: ball (b), inner ring (i), outer ring (o), cage (c), cage pocket (p), and ordinal number (j) for balls. The vibration characteristics of each component are analyzed below [33, 34].

Fig. 1 Interaction among the bearing components
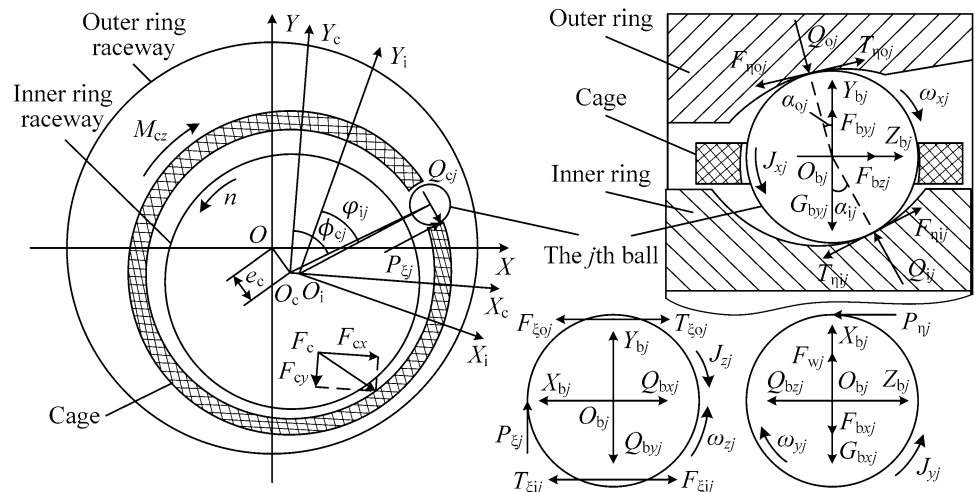
2.1.1 Differential equations of vibrations on ceramic ball

As an important component of an angular contact ball bearing, the balls contact all components, i.e., the cage, inner, and outer rings. It is supposed that all ceramic balls are equal in mass and size, and the sizes of the cage pockets, which are distributed uniformly along the circumference, are the same.

In Fig. 1, α_{ij} and α_{oj} are the contact angles between the jth ceramic ball and inner and outer raceways; Q_{ij} and Q_{oj} are the normal contact forces between the jth ceramic ball and inner and outer raceways, respectively; $T_{\eta ij}$, $T_{\eta oj}$, $T_{\xi ij}$, and $T_{\xi oj}$

speed of the inner ring; ϕ_{cj} is the position angle of the jth ceramic ball relative to the cage; φ_{ij} is the position angle of the jth ceramic ball relative to the inner ring.

The normal contact forces can be obtained through Hertz contact theory [35], and the traction forces can be calculated [36] by $\eta V_c S_c / h_c$, where η is the lubricant viscosity; V_c is the relative velocity of the ball and raceways; S_c is the contact area; and h_c is the film thickness. For the detailed calculation of the other forces, please refer to Ref. [33]. The differential equation for the vibration of the jth ceramic ball can be described as

$$F_{\xi oj} - T_{\xi oj} - F_{\xi ij} + T_{\xi ij} - F_{bxj} - G_{bxj} - Q_{bxj} + F_{wj} = m_b \ddot{x}_{bj}$$

$$(F_{\eta ij} - T_{\eta ij}) \sin \alpha_{ij} - (F_{\eta oj} - T_{\eta oj}) \sin \alpha_{oj} + Q_{ij} \cos \alpha_{ij} - Q_{oj} \cos \alpha_{oj} + F_{byj} - G_{byj} - Q_{byj} + P_{\xi j} = m_b \ddot{y}_{bj}$$

$$(F_{\eta ij} - T_{\eta ij}) \cos \alpha_{ij} - (F_{\eta oj} - T_{\eta oj}) \cos \alpha_{oj} - Q_{ij} \sin \alpha_{ij} + Q_{oj} \sin \alpha_{oj} + F_{bzj} - Q_{bzj} - P_{\eta j} = m_b \ddot{z}_{bj}$$

$$(T_{\eta ij} - F_{\eta ij} + T_{\eta oj} - F_{\eta oj}) \frac{D_W}{2} - J_{xj} \dot{\omega}_{xj} = I_b \dot{\omega}_{bxj} + I_b \omega_{byj} \dot{\theta}_{bj} \tag{1}$$

$$\left[(F_{\xi ij} - T_{\xi ij}) \sin \alpha_{ij} + (F_{\xi oj} - T_{\xi oj}) \sin \alpha_{oj} - P_{\eta j} \right] \frac{D_W}{2} - J_{yj} \dot{\omega}_{yj} = I_b \dot{\omega}_{byj} + I_b \omega_{bxj} \dot{\theta}_{bj}$$

$$\left[(T_{\xi ij} - F_{\xi ij}) \cos \alpha_{ij} + (T_{\xi oj} - F_{\xi oj}) \cos \alpha_{oj} - P_{\xi j} \right] \frac{D_W}{2} - J_{zj} \dot{\omega}_{zj} = I_b \dot{\omega}_{bzj}$$

are the traction forces of the contact surface between the jth ceramic ball and raceways; Q_{cj} is the collision force between the jth ceramic ball and cage; Q_{bxj}, Q_{byj}, and Q_{bzj} are the decomposition components of Q_{cj}, which are acting on the jth ceramic ball; G_{bxj} and G_{byj} are the decomposition components of the gravity of the jth ceramic ball; $P_{\eta j}$ and $P_{\xi j}$ are the friction forces acting on the surface of the jth ceramic ball, including rolling and sliding friction forces; F_{bxj}, F_{byj}, and F_{bzj} are the components of the hydrodynamic force acting on the center of the jth ceramic ball; $F_{\eta ij}$, $F_{\eta oj}$, $F_{\xi ij}$, and $F_{\xi oj}$ are the hydrodynamic friction forces at the lubricant inlet of the contact zone of ball and raceways; F_{wj} is the aerodynamic resistance acting on the jth ceramic ball by gas–oil mixture; J_{xj}, J_{yj}, and J_{zj} are the components of the moment of inertia for the jth ceramic ball; ω_{xj}, ω_{yj}, and ω_{zj} are the components of the spin angular velocity of the jth ceramic ball; e_c is the relative eccentricity of the cage center; n is the rotation

where D_W is the diameter of the ceramic ball; m_b is its mass; $\ddot{x}_{bj}$, $\ddot{y}_{bj}$, and $\ddot{z}_{bj}$ are the displacement accelerations of the barycenter of the jth ball; $\dot{\omega}_{xj}$, $\dot{\omega}_{yj}$, and $\dot{\omega}_{zj}$ are the components of the spin angular acceleration of the jth ball; ω_{bxj}, ω_{byj}, and ω_{bzj} are the angular velocities of the jth ball; $\dot{\omega}_{bxj}$, $\dot{\omega}_{byj}$, and $\dot{\omega}_{bzj}$ are the angular accelerations of the jth ball; $\dot{\theta}_{bj}$ is the orbit speed of the jth ball; I_b is the moment of inertia of the ball.

2.1.2 Differential equations of vibrations on cage

During the operation of the bearing, the cage contacts only the ball, and friction and impact are generated. In Fig. 1, F_{cx}, and F_{cy} are the components of the hydrodynamic force, F_c, acting on the cage; M_{cz} is the friction moment acting on the cage. The differential equation for the vibration of the cage can be described as

$$\sum_{j=1}^{N} (Q_{cxj} - P_{\xi j} \sin \varphi_{cj}) + F_{cx} = m_c \ddot{x}_c$$

$$\sum_{j=1}^{N} (Q_{cyj} + P_{\xi j} \cos \varphi_{cj}) + F_{cy} = m_c \ddot{y}_c$$

$$\sum_{j=1}^{N} (Q_{czj} + P_{\eta j}) = m_c \ddot{z}_c$$

$$\sum_{j=1}^{N} (P_{\eta j} + Q_{czj})\left(\frac{d_m}{2}\cos\varphi_{cj} - \frac{D_W}{2}\sin\varphi_{cj}\right) = I_{cx}\dot{\omega}_{cx} - (I_{cy} - I_{cz})\omega_{cy}\omega_{cz}$$

$$\sum_{j=1}^{N} (P_{\eta j} + Q_{czj})\left(\frac{d_m}{2}\sin\varphi_{cj} + \frac{D_W}{2}\cos\varphi_{cj}\right) = I_{cy}\dot{\omega}_{cy} - (I_{cz} - I_{cx})\omega_{cz}\omega_{cx}$$

$$\sum_{j=1}^{N} \left[P_{\xi j}\frac{D_W}{2} + Q_{cxj}\left(\frac{d_m}{2}\cos\varphi_{cj} - \frac{D_W}{2}\sin\varphi_{cj}\right) - Q_{cyj}\left(\frac{d_m}{2}\sin\varphi_{cj} + \frac{D_W}{2}\cos\varphi_{cj}\right)\right] + M_{cz} = I_{cz}\dot{\omega}_{cz} - (I_{cx} - I_{cy})\omega_{cx}\omega_{cy}$$

$$(2)$$

where m_c is the mass of the cage; d_m is the pitch diameter of the bearing; N is the number of the ceramic ball; Q_{cxj}, Q_{cyj}, and Q_{czj} are the decomposition components of Q_{cj}, which are acting on the cage; $\ddot{x}_c$, $\ddot{y}_c$, and $\ddot{z}_c$ are the displacement accelerations of the barycenter of the cage; ω_{cx}, ω_{cy}, and ω_{cz} are the angular velocities of the cage; $\dot{\omega}_{cx}$, $\dot{\omega}_{cy}$, and $\dot{\omega}_{cz}$ are the angular accelerations of the cage; I_{cx}, I_{cy}, and I_{cz} are the moments of inertia of the cage.

2.1.3 Differential equations of vibrations on inner ring

Vibrations of the inner ring are mainly caused by the contact friction between ball and inner ring. The differential equation for the vibration of the inner ring can be described as

are the displacement accelerations of the barycenter of the inner ring; ω_{ix}, ω_{iy}, and ω_{iz} are the angular velocities of the inner ring; $\dot{\omega}_{ix}$, $\dot{\omega}_{iy}$, and $\dot{\omega}_{iz}$ are the angular accelerations of the inner ring; I_{ix}, I_{iy}, and I_{iz} are the moments of inertia of the inner ring; k_i is the inner ring raceway curvature radius coefficient; $r_{ij} = (d_m - D_W k_i \cos\alpha_{ij})/2$ is the raceway radius of the inner ring.

2.1.4 Radiation sound pressure of FCACBB

The study of the noise of rolling bearings is based on the theory of acoustics, sound radiation, and propagation. The radiation noise of a FCACBB exhibits all the attributes of sound. The sound radiation comes from the surface vibration

$$F_{ix} + \sum_{j=1}^{N} \left[(F_{\xi ij} - T_{\xi ij})\cos\phi_{ij} + (T_{\eta ij} - F_{\eta ij})\sin\alpha_{ij}\sin\phi_{ij} - Q_{ij}\cos\alpha_{ij}\sin\phi_{ij} \right] = m_i \ddot{x}_i$$

$$F_{iy} + \sum_{j=1}^{N} \left[(T_{\xi ij} - F_{\xi ij})\sin\phi_{ij} + (T_{\eta ij} - F_{\eta ij})\sin\alpha_{ij}\cos\phi_{ij} - Q_{ij}\cos\alpha_{ij}\cos\phi_{ij} \right] = m_i \ddot{y}_i$$

$$F_{iz} + \sum_{j=1}^{N} \left[(T_{\eta ij} - F_{\eta ij})\cos\alpha_{ij} + Q_{ij}\sin\alpha_{ij} \right] = m_i \ddot{z}_i$$

$$(3)$$

$$M_{ix} + \sum_{j=1}^{N} \left[Q_{ij}\sin\alpha_{ij} + (T_{\eta ij} - F_{\eta ij})\cos\alpha_{ij} \right] r_{ij}\cos\phi_{ij} - \sum_{j=1}^{N} \left[(T_{\xi ij} - F_{\xi ij})\frac{D_W}{2}k_i\sin\alpha_{ij}\sin\phi_{ij} \right] = I_{ix}\dot{\omega}_{ix} - (I_{iy} - I_{iz})\omega_{iy}\omega_{iz}$$

$$M_{iy} + \sum_{j=1}^{N} \left[Q_{ij}\sin\alpha_{ij} + (T_{\eta ij} - F_{\eta ij})\cos\alpha_{ij} \right] r_{ij}\sin\phi_{ij} + \sum_{j=1}^{N} \left[(T_{\xi ij} - F_{\xi ij})\frac{D_W}{2}k_i\sin\alpha_{ij}\cos\phi_{ij} \right] = I_{iy}\dot{\omega}_{iy} - (I_{iz} - I_{ix})\omega_{iz}\omega_{ix}$$

where m_i is the mass of the inner ring; F_{ix}, F_{iy}, and F_{iz} are the external loads acting on the inner ring; M_{ix} and M_{iy} are the external torques acting on the inner ring; $\ddot{x}_i$, $\ddot{y}_i$, and $\ddot{z}_i$

of the bearing components. Therefore, the sound pressure emitted from each component at the field point is calculated

by the Helmholtz sound wave equation, boundary condition, and Sommerfeld radiation condition in the sound field.

When the bearing rotates at a certain speed, the contact between the components of the bearing results in friction and impact vibrations and then leads to friction and impact noise. Assuming that the propagation of sound waves is conducted in an isotropic and homogeneous medium, the wave equation of sound pressure can be described with the Helmholtz equation as [37]

$$\nabla^2 p(P) = \frac{1}{c_0^2} \frac{\partial^2 p(P)}{\partial t^2} = -k^2 p(P) \tag{4}$$

where ∇^2 denotes the Laplace operator, $p(P)$ is the sound pressure, c_0 is the sound velocity, $k = 2\pi f_0/c_0$ is the wave number, and f_0 is the acoustic frequency. The Helmholtz integral equation used in the calculation of the acoustic field around the vibrating component with boundary surface S and outward normal n can be expressed as [38, 39]

$$C(P)p(P) = \int_S [p(M)\frac{\partial G(R,k)}{\partial n(M)} + iz_0 k v_n(M) G(R,k)] dS(M) \tag{5}$$

where P is an arbitrary point in the space, M is the configuration point on the surface of the sound source component, and $R = |P - M|$ is the distance between P and M, $i = \sqrt{-1}$ is an imaginary unit, $z_0 = \rho_0 c_0$ is the characteristic impedance of the medium, ρ_0 denotes the density of the medium, v_n indicates the normal surface velocity, $G(R, k) = e^{-ikR}/R$ is the Green's function, and $C(P)$ is the position coefficient of P and is given in [40]

$$C(P) = \begin{cases} 1 & P \in V \\ 4\pi + \int_S \left[\frac{\partial (1/R)}{\partial n}\right] dS & P \in S \\ 0 & P \notin (V \cup S) \end{cases} \tag{6}$$

where V is the external space of the sound source surface. The value of $C(P)$ is only related to the topological structure of the sound source, but is independent of the frequency. When the boundary element method is applied to Eq. (5), then under the fluid–solid boundary condition and Sommerfeld radiation condition, the following system of equations can be obtained:

$$\mathbf{E} \cdot \mathbf{p}_S - \mathbf{K} \cdot \mathbf{p}_S = \mathbf{H} \cdot \mathbf{v}_n \tag{7}$$

where $\mathbf{E}$ is a diagonal matrix including the geometrical data, $\mathbf{K}$ and $\mathbf{H}$ are square matrices, $\mathbf{p}_S$ is the column vector of the sound pressure on structural surface S, and $\mathbf{v}_n$ is the column vector of the normal velocity containing all the nodes, which can be derived from Eqs. (1)–(3). The number of elements in matrices $\mathbf{E}$, $\mathbf{K}$, and $\mathbf{H}$ is the square of all the contact points in the bearing. Then, the field sound pressure based on the surface vibration of the components at an arbitrary point
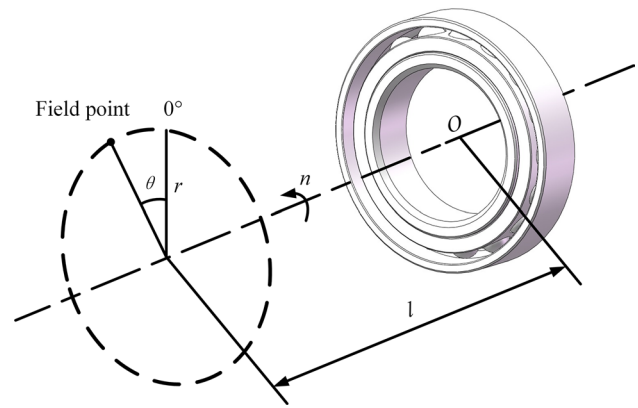

Fig. 2 Schematic diagram of field point coordinates

may be determined by substituting the calculated surface pressures into Eq. (4) to yield

$$p(P) = \mathbf{K}_e^{\mathbf{T}} \cdot \mathbf{p} + \mathbf{H}_e^{\mathbf{T}} \cdot \mathbf{v}_n \tag{8}$$

where $p(P)$ is the exterior field sound pressure and superscript $\mathbf{T}$ denotes the transpose of the vector. The elements of vectors $\mathbf{K}_e^{\mathbf{T}}$ and $\mathbf{H}_e^{\mathbf{T}}$ are the rows of matrices $\mathbf{K}$ and $\mathbf{H}$, respectively, divided by 4π.

2.2 Characterization of sound field

2.2.1 Sound pressure level of radiation noise

Generally, sound pressure level (SPL) is the main index used to assess and analyze sound radiation. The SPL is defined as

$$\text{SPL}(P) = 20\log\frac{p(P)}{p_{\text{ref}}} \tag{9}$$

where $SPL(P)$ is the SPL of the field point P and p_{ref} is the reference sound pressure.

In order to analyze the sound field distribution characteristics of FCACBBs, an arbitrary field point is selected to calculate its SPL. At a certain preload, the centers of all ceramic balls are assumed to be in the same plane, which is defined as the bearing plane. The bearing axis is perpendicular to the bearing plane. As shown in Fig. 2, the bearing plane is placed vertically. Assuming that the bearing outer ring is fixed and the bearing inner ring rotates with the speed of n, a cylindrical coordinate system is applied to analyze the SPL of the sound field. The origin of the coordinate system lies at the intersection point between the bearing axis and the bearing plane. The 12 o'clock direction is defined as position angle with 0°. The bearing rotation direction is the positive direction of the position angle. The location of field point P can be expressed as

$$P = P(\theta, r, l) \tag{10}$$

where θ represents the position angle of the field point, r represents radial distance from the field point to the bearing axis, and l represents the axial distance from the field point to the bearing plane.

The SPL of bearing radiation noise is not only directly related to the position of the field point, but also related to the working speed of bearings. Therefore, the SPL of the arbitrary field point x can be expressed as

$$SPL(P) = f(n, \theta, r, l) \tag{11}$$

where n represents the rotational speed of the bearing inner ring and f represents that the SPL of any field point is the function of n, θ, r, and l.

It can be seen from Eq. (5) that the SPL is related to the velocity v_n and the distance R. The velocity v_n which changes periodically along the circumference of the bearing is related to the bearing rotational speed n, i.e., the angular velocity ω. The velocity v_n can be derived from Eqs. (1)–(3). The distance R can be calculated by

$$R = \sqrt{r^2 + r_i^2 - 2rr_i\cos(\theta - \phi) + l^2} \tag{12}$$

where r_i represents the distance from the contact point to the bearing axis

The sound pressure can be obtained by substituting the velocity v_n and the distance R into Eqs. (5)–(8), and then, the SPL can be further calculated by Eq. (9). Thus, the function f is obtained, i.e., Eq. (11) is derived.

2.2.2 Directivity parameter of sound field

In order to analyze the distribution characteristics of the sound field of the FCACBB, the directivity of the sound field is used to characterize the regularities of distribution of the sound field. The directivity of the sound field is defined as the nonuniform distribution of the SPL in the circumferential direction with a given radius r. The

Table 1 Structural parameters of the ceramic bearing

Parameter	Value
Bearing outside diameter (mm)	75
Inner ring bore diameter (mm)	45
Bearing width (mm)	16
Cage outside diameter (mm)	63.5
Pocket diameter (mm)	8.9
Cage width (mm)	14
Ball diameter (mm)	8.731
Ball number	17
Initial contact angle (°)	15

directivity of sound field can be described by two parameters. One is directivity angle (DA), and the other is directivity level (DL). They are collectively referred to as directivity parameters of the sound field and can be defined as

$$DA = \theta_{SPL}(n, r, l) \tag{13}$$

$$DL = \frac{SPL_{max}(n, r, l)}{SPL_{ave}(n, r, l)} \tag{14}$$

where SPL_{max} represents the maximum value of the SPL in the whole circumferential direction or a certain range of the position angle with a given n, r, and l; SPL_{ave} represents the average value of the SPL in the whole circumferential direction with a radius r; θ_{SPL} represents the position angle where the SPL_{max} appears.

The directivity of the sound field is related to the rotational speed, radial distance, and axial distance. The DA gives the orientation of directivity, and the DL represents the degree of directivity. The greater value of the DL can get the more obvious the directivity.

In addition, the difference value (DV) between the maximum SPL and minimum SPL in the whole circumferential direction can reflect the difference of noise distribution in the circumferential direction, and it can be calculated by

$$DV = SPL_{max}(n, r, l) - SPL_{min}(n, r, l) \tag{15}$$

where SPL_{max} and SPL_{min} are only the maximum and minimum values of the SPL in the whole circumferential direction.

2.3 Radiation noise

The structural parameters of the bearing model match with the H7009C bearing and are shown in Table 1. The
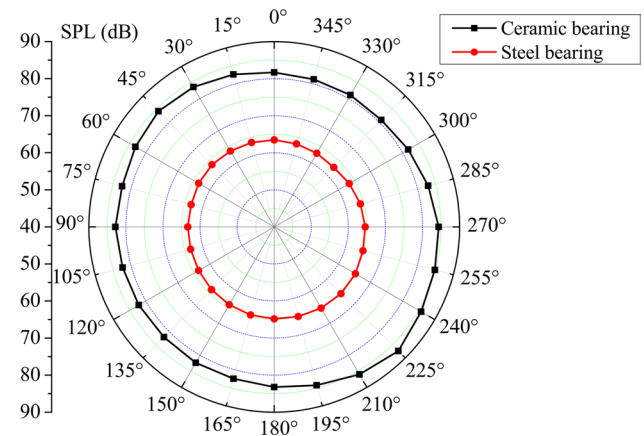
Fig. 3 Calculated results of the circumferential direction at the speed of 18,000 r min^{-1}

materials of the bearing rings, balls, and cage were set as zirconia (ZrO_2) ceramics, silicon nitride (Si_3N_4) ceramics, and polyetheretherketone (PEEK) resins, respectively. The preload and rotational speeds of the FCACBB were set as 350 N and 18,000 r min^{-1}. The bearing operated without external load and with excellent lubrication state. The air density and the sound velocity were set to 1.225 kg m^{-3} and 340 m s^{-1}, respectively. The reference sound pressure was 2×10^{-5} Pa. The SPLs of 24 field points on a circle parallel to the bearing plane were calculated, and the field points were evenly distributed along the circumferential direction with the interval of 15°. The distance from the field point plane to the bearing plane (axial distance) was 50 mm, and the distance from the field point to the bearing axis (radial distance) was 210 mm. Here, the 12 o'clock direction was defined as 0° or point 1, and the rest of field points were numbered counterclockwise in a sequence.

The radiation noise can be calculated by Eqs. (1)–(8), and the sound field characteristics can be analyzed by Eqs. (9)–(15). The frequency range of calculation was set from 0 to 20 kHz. The calculated results are shown in Fig. 3.

In Fig. 3, the annular coordinate shows circumferential PAs, and the concentric circles represent SPLs. The ceramic bearing represents FCACBB which has the same dimensions with the steel bearing. It can be seen that the FCACBB has larger radiation noise than the traditional steel bearing and the SPLs show differences in the circumferential direction. The sound field of the FCACBB has an obvious directivity in the circumferential direction, but the sound field directivity of the traditional steel bearing is not obvious. The SPLs have a maximum value at the lower semicircle toward the rotation direction. The DV of the FCACBB is 6.53 dB, and that of the steel bearing is 2.76 dB. In addition, there is a local large value in the
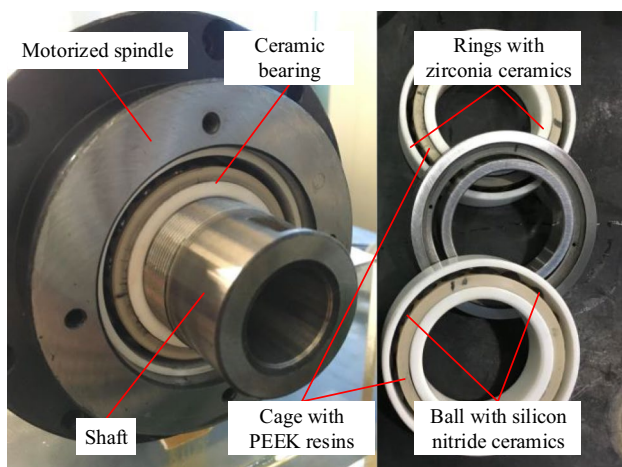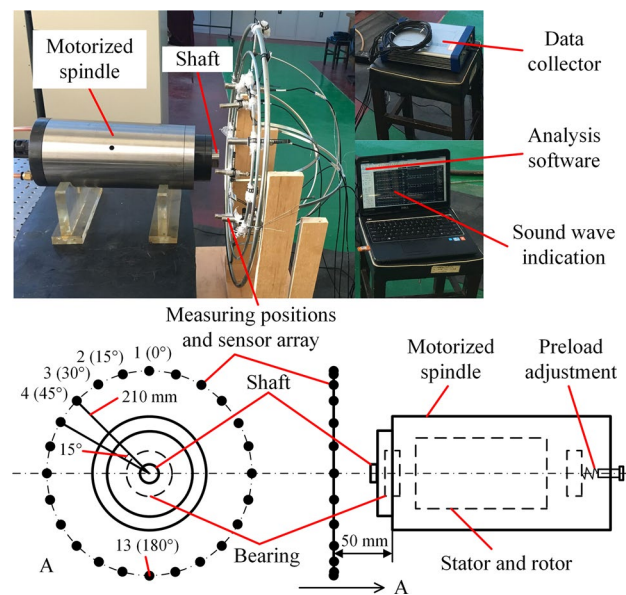

Fig. 5 Experimental scheme

upper left semicircle, and its PA can be called local DA. Therefore, there are two local directivity directions in the sound field of the FCACBB, and the direction with the maximum SPL is the directivity direction of the whole sound field. The DL in the directivity direction of the whole sound field is greater than that in other directions, which indicates that the degree of directivity of the whole sound field is more obvious than that of the local one.

3 Experimental verification

A test rig for measuring the bearing noise was built. The ambient temperature in the laboratory was 26 °C. The background noise during the experiment was lower than 45 dB. The type of the measured bearing was H7009C, and it was assembled in a motorized spindle with the type of 150MD18Y14.5. The bearing had the same rotational speed as the rotor due to interference fit between bearing inner ring and shaft. The rated speed of the motorized spindle is 18,000 r min^{-1}. The bearing rings, balls, and cage were made of ZrO_2 ceramics, Si_3N_4 ceramics, and PEEK resins, respectively. The structural parameters of the bearing are listed in Table 1. The motorized spindle and its supporting bearings are shown in Fig. 4.

A water cooling system and an oil–gas lubrication system were applied to the cooling and lubrication of the motorized spindle. The cooling temperature was set at a constant of 18 °C. The engine oil with 30# was used for bearing lubrication. The pressure of air was 0.28 MPa. The flow rates of lubrication oil and cooling water were set to 0.025 mL min^{-1}

Fig. 4 Motorized spindle and ceramic bearings
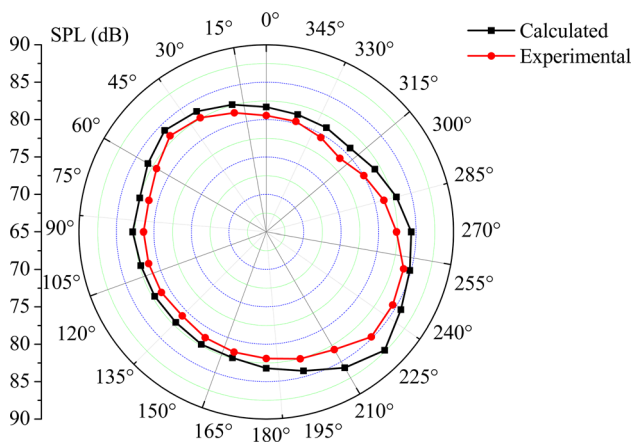
Fig. 6 Comparison between calculated and experimental results at the speed of 18,000 r min^{-1}
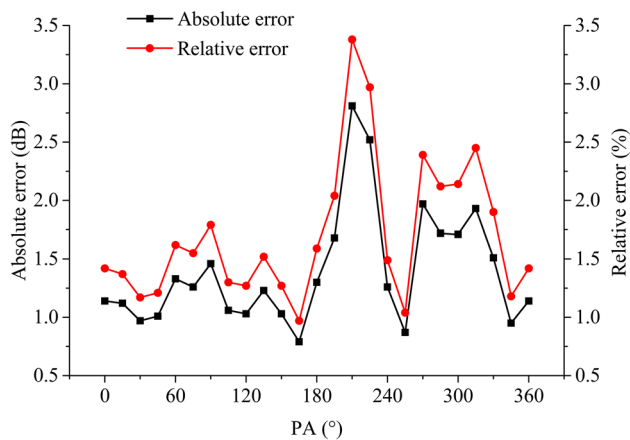
Fig. 7 Absolute error and relative error at the speed of 18,000 r min^{-1}

and 5.0 L min^{-1}. The preload of bearings was adjusted to 350 N. The motorized spindle was driven by built-in motor, and it operated at a steady state during the test.

As shown in Fig. 5, the 24 measuring points were selected to verify the accuracy of the calculation and analyze the radiation noise of the FCABB applied in the motorized spindle. The axis of the spindle (bearing) was placed in the horizontal plane. All points were arranged in a plane of the front of the spindle (bearing), and the plane was 50 mm away from the bearing plane. The measuring points were evenly distributed in the circumferential direction with 210 mm away from the center line of the bearing. The angle interval between the adjacent two measuring points was 15°. The first measuring point was above the motorized spindle (bearing), and the direction was set to 0° which was the same position as the simulation field point. The 24 measuring points were arranged in counterclockwise direction and numbered in a sequence.

The sound pressure sensors (IVN9206-I) with sensitivities from 50 to 54.5 mV Pa^{-1} were placed at the measuring points. The sound pressure signals of each measuring point were collected by a data collector (INV3018C). The sampling frequency and sampling time were 51.2 kHz and 10 s, respectively. The collected data were sent to the computer for further processing the sound pressure data and analyze the radiation sound field characteristics of the FCACBB.

With the spindle spun counterclockwise at 18,000 r min^{-1}, the calculated values and experimental results in the circumferential direction are shown in Fig. 6.

As shown in Fig. 6, it can be seen that the calculated and experimental SPLs have similar change trend along the circumferential direction, and all experimental results are relatively low compared with calculated values. The primary reason for the case is that the transmission of the radiation noises of the FCACBB is only considered under the condition of the ideal sound propagation and equivalent analysis in the calculated model, while the sound waves get more attenuation and absorption due to the barrier of housing of the motorized spindle during the experiment. As shown in Fig. 7, the relative error of calculation is from 0.97% (0.79 dB) to 3.38% (2.81 dB) in the circumferential direction at the speed of 18,000 r min^{-1}. The average relative error is 1.71% (1.40 dB). The minimum error presents at the PA of 165°, and the maximum error appears at the PA of 210°. According to these results, the calculation model has accurate calculation results in the circumferential direction.

In order to further verify the calculation accuracy under different speeds, the spindle spun counterclockwise at 3000 r min^{-1}, 6000 r min^{-1}, 9000 r min^{-1}, 12,000 r min^{-1}, 15,000 r min^{-1}, and 18,000 r min^{-1}, and the comparison between the calculated values and experimental results at the measuring points 1, 7, 13, and 19 is shown in Fig. 8.

In Fig. 8, the black lines with square legends show the variation trend of calculated values with the speed at points 1, 7, 13, and 19, while the red lines with circle legends show the variation trend of experimental results with the speed at points 1, 7, 13, and 19, respectively. It is clearly displayed that the calculated values have almost the similar variation tendencies and match well with the experimental results under all speeds. As shown in Fig. 9, the maximum error reaches 2.32 dB (2.99%) at point 19 at 15,000 r min^{-1} and the minimum error is only 0.77 dB (1.08%) at point 13 at 3000 r min^{-1}. However, the calculated values are also slightly larger than the experimental results. Compared with the SPL of the radiation noise, the error values are small and acceptable. So the calculated model has a high calculation accuracy. The proposed radiation noise model can be applied in the analysis of the sound field distribution characteristics of the radiation noise of the FCACBB and further ascertaining the acoustical properties of the FCACBB.
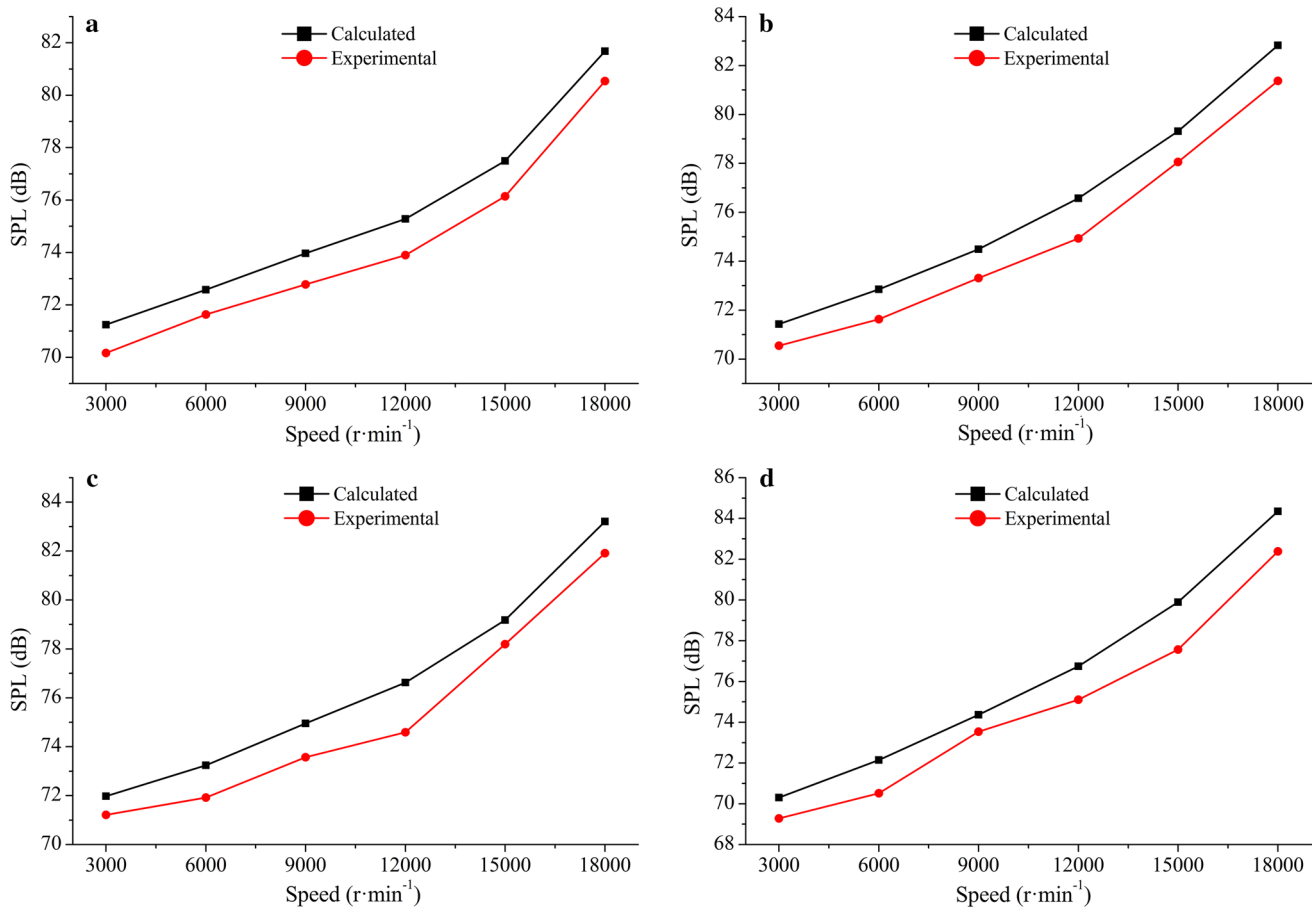
Fig. 8 Comparison between calculated values and experimental results at **a** point 1, **b** point 7, **c** point 13, and **d** point 19

4 Results and discussion

The distribution of the sound field is analyzed by the calculated results. The radiation noise of a FCACBB with the same parameter as the H7009C in Table 1 is calculated by the proposed model. Also, the materials of the bearing are the same as previously described. The distribution of the sound field of the FCACBB is analyzed in more detail in the following sections.

4.1 Distribution of sound field in circumferential direction

Rotational speed is an important factor affecting the bearing noise. In order to obtain more detailed information about bearing radiation noise, the directivity of sound field in circumferential direction was studied under different rotational speeds. According to the introduction of Sect. 3, the 24 field points were selected to analyze the characteristics of the radiation noise in circumferential direction. The distance from the field point to the bearing axis was 210 mm. Assuming that the bearing operated steadily with the axial preload

of 350 N, the directivity of sound field was explored at the rotational speed of 3000 r min^{-1}, 6000 r min^{-1}, 9000 r min^{-1}, 12,000 r min^{-1}, 15,000 r min^{-1}, and 18,000 r min^{-1}. The distribution of sound field in circumferential direction under different speeds is shown in Fig. 10.

As shown in Fig. 10, the radiation noise increases with increasing the rotational speed and it has the maximum radiation noise at rated speed. In the circumferential direction with the same distance from field point to bearing axis, there is an uneven distribution of the sound field. The SPLs have a larger value at the upper left semicircle and at the right lower semicircle. A great impact noise caused by the ceramic ball and cage is in an angle range of 0–60° (upper left semicircle), which can be called impact load zone. A great friction noise caused by the ceramic ball and rings is in an angle range of 180–240° (right lower semicircle), which is defined as friction load zone. The radiation noise in the impact load zone is slightly higher than that in the friction load zone at a low rotational speed. While with the increase in the rotational speed, the variation of the radiation noise in the friction load zone increases rapidly and becomes gradually larger than the radiation noise in the impact load zone.
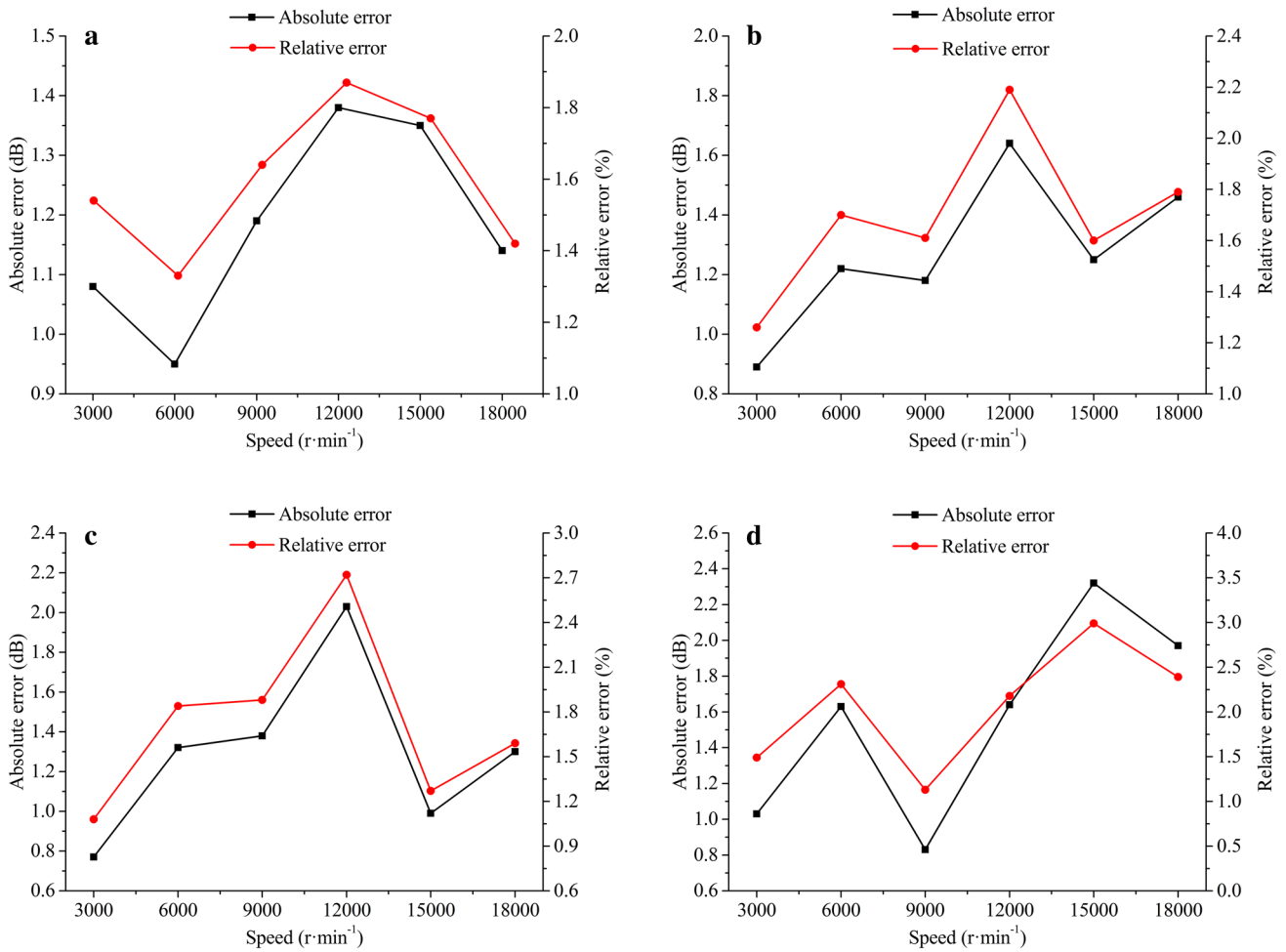
Fig. 9 Absolute error and relative error at points **a** 1, **b** 7, **c** 13, and **d** 19
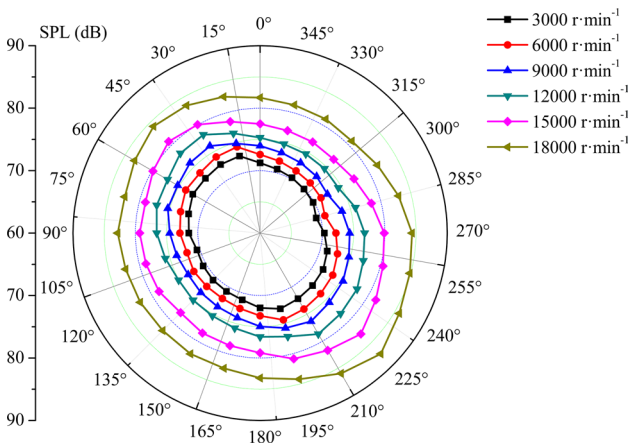

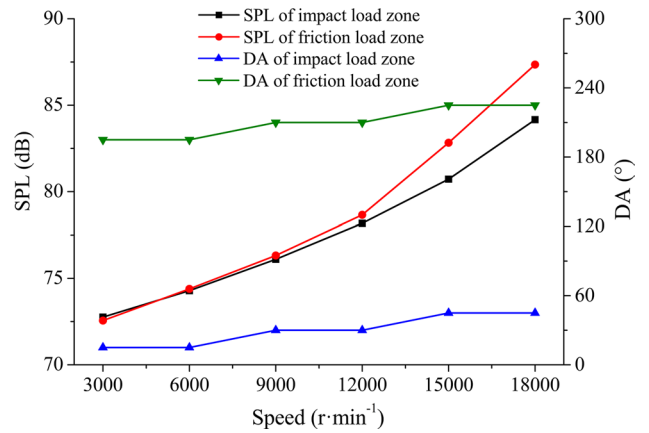**Fig. 10** Distribution of sound field in circumferential direction under different speeds

Fig. 11 Maximum SPL in the impact load zone and friction load zone and their DA under different speeds
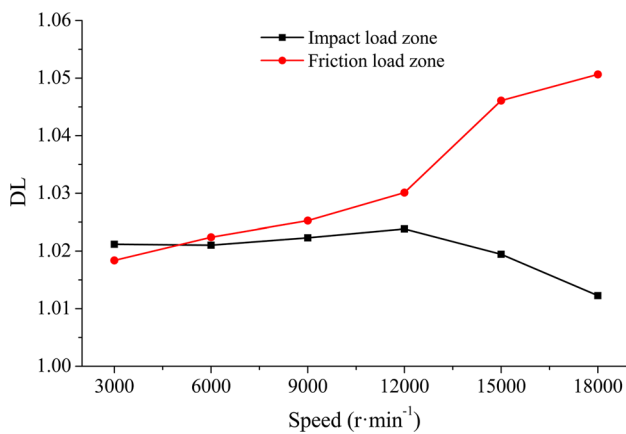
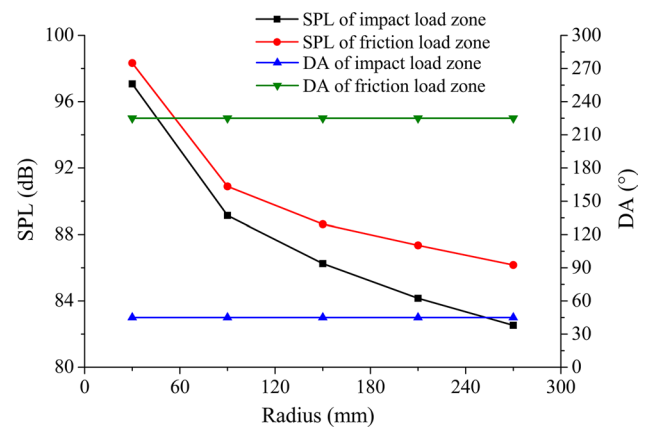Fig. 12 Trend of the DL with the rotational speed

Fig. 14 Maximum SPL in the impact load zone and friction load zone and their DA at different radii
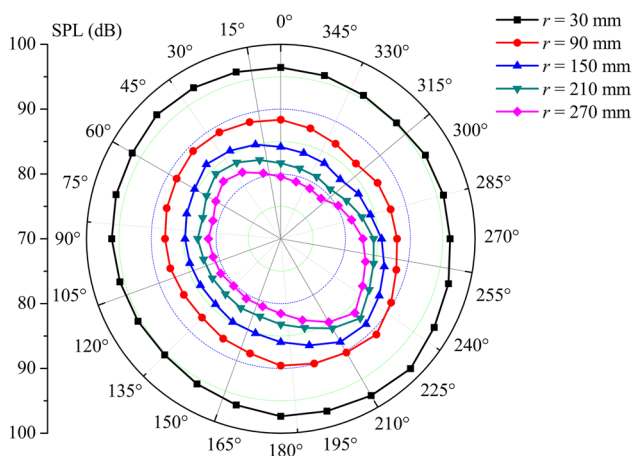

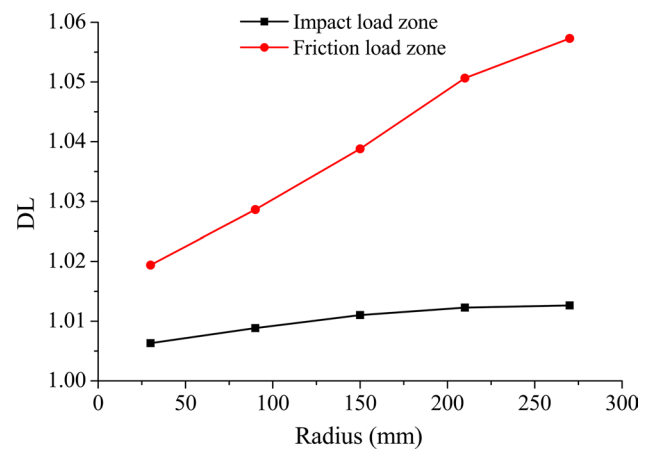Fig. 13 Distribution of sound field in radial direction of the bearing

Fig. 15 Trend of the DL with the radius

In Fig. 11, it can be seen that the SPLs are lower in the friction load zone than in the impact load zone at the speed of 3000 r min⁻¹, while the SPLs of the friction load zone are lager than that in the impact load zone in a speed range of 3000–18,000 r min⁻¹, and their difference value will be enlarged with increasing the speed. As a whole, the DA of impact load zone gradually moves from 15° to 45° and the DA of friction load zone gradually moves from 195° to 225° with the increase in the speed from 3000 to 18,000 r min⁻¹. The DAs in impact load zone and friction load zone have the same pace of change, and they always maintain a difference angle of 180°. With increasing the rotational speed, the inner ring of the bearing rotates counterclockwise, resulting in the bearing eccentricity toward the lower right, so the friction load zone moves upward along with the rotation direction. Meanwhile, the impact load zone moves downward along with the rotation direction.

As shown in Fig. 12, the DL in impact load zone has the small fluctuation in a speed range of 3000–12,000 r min⁻¹,

and then, it is obviously reduced under the speed of 15,000 r min⁻¹ and 18,000 r min⁻¹. However, the DL in friction load zone increases with increasing rotational speed. It indicates that the directivity of sound field in friction load zone becomes more and more obvious and the directivity of sound field in impact load zone is weakened when the speed increases from 3000 to 18,000 r min⁻¹. However, the directivity of sound field is enhanced in the whole circumferential direction with the increase in the rotational speed. The directivity of sound field seems to show some certain regularities. With the increase in the rotational speed, the centrifugal force of the ball increases rapidly and varies due to the bearing eccentricity. The direction of the complex resultant force acting on the ball varies correspondingly. Therefore, the increase in rotational speed leads to the increase in friction force, further resulting in the increase in friction noise. On the other hand, the friction is smaller and the impact is larger with the lower-speed bearing. Therefore, the impact noise is

relatively greater than the friction noise at low speed. With the increase in friction, the impact effect is weakened relative to friction effect, and the dominant noise in the impact load zone has also changed from the impact noise to the friction noise.

4.2 Distribution of sound field in radial direction

The directivity of the sound field at different radial distances is a significant factor to show the sound attenuation with the radial distance. In order to analyze the directivity of sound field in circumferential direction with different radial distances, the field points were located on concentric circles of different radii. The bearing operated without external load at the rotational speed of 18,000 r min^{-1}. The other parameters remain unchanged. The directivity of sound field was discussed at a set of concentric circles with the radius of 30 mm, 90 mm, 150 mm, 210 mm, and 270 mm. The distribution of sound field in circumferential direction under different radii is shown in Fig. 13.

Figure 13 shows the SPL in circumferential direction varying with the radius of concentric circle. The radiation noise decreases nonlinearly with the increase in the radius of sound radiation in the radial direction of bearing. And the change values are not uniform at different directions, leading to large fluctuation at circumferential direction with a big radius. The SPLs of friction load zone have relatively small changes compared with that of impact load zone. The maximum SPL in the friction load zone is larger than that in the impact load zone. The DAs in both of load zones are constant values. The DA in impact load zone stays at 45°, and the DA in friction load zone stays at 225°. It shows that the variation of radius does not change the PA of maximum SPL. This information is also shown in Fig. 14. In addition, according to the circumferential
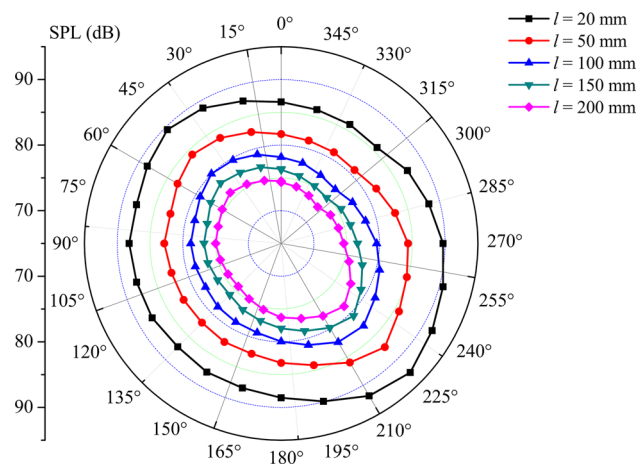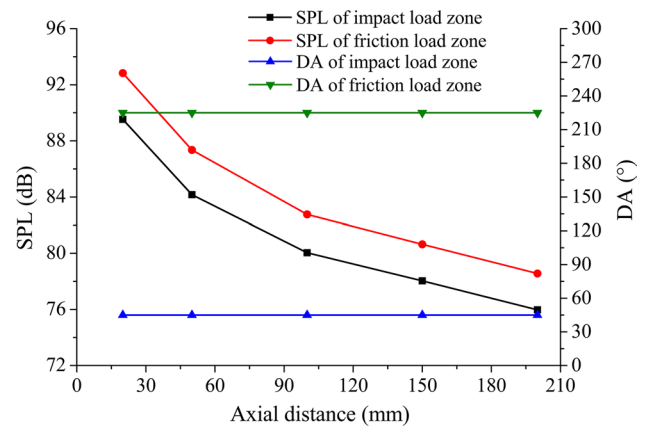

Fig. 17 Maximum SPL in the impact load zone and friction load zone and their DA at different axial distances

distributions of SPLs, the increase in the radius highlights the directivity of sound field. It can be seen from Fig. 15 that the DL curve in the friction load zone is above that in the impact loading zone and they both raise with the radius. However, the values increase slower in impact load zone than in friction load zone. The trend of DL curves indicates that the directivity of sound field strengthens with increasing the radius. The reason for the change of the sound field is that the sound radiation decays with the increase in distance, and the attenuation degree is different in different directions.

4.3 Distribution of sound field in axial direction

The directivity of the sound field at different axial distances is also a key factor to show the sound attenuation with the axial distance. In order to study the axial distribution characteristics of the sound field of the FCACBB, the field points were placed in the circumferential direction with a radius
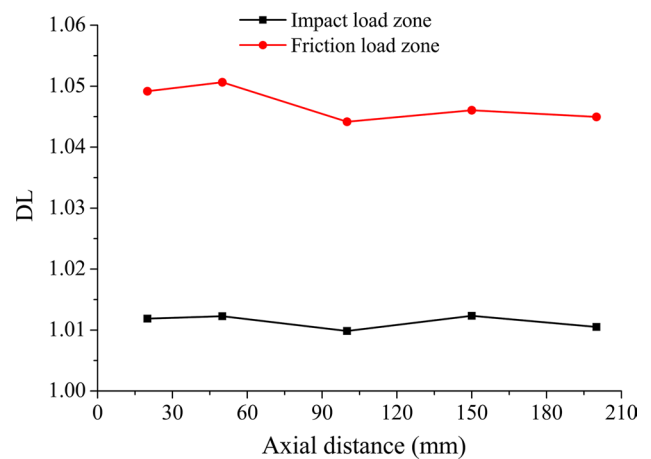

Fig. 16 Distribution of sound field in axial direction of the bearing

Fig. 18 Trend of the DL with the axial distance
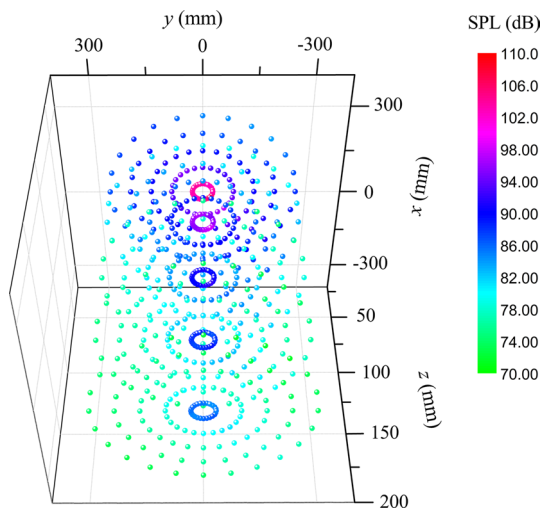
Fig. 19 Distribution of sound field of the FCACBB

Fig. 20 The SPL_{max} of radiation noise at different field points

of 210 mm. The directivity of sound field was analyzed at the axial distance of 20 mm, 50 mm, 100 mm, 150 mm, and 200 mm. The other parameters were the same as before. The distribution of sound field in circumferential direction under different axial distances is shown in Fig. 16.

As shown in Figs. 16 and 17, the SPL gradually decreases with the axial distance, and the two DAs still stay at 45° and 225°. It shows that the DAs are not affected by the axial distance just like it is not affected by the radial distance. The attenuation scale of the maximum SPL in the impact load zone is almost the same as that in the friction load zone. Figure 18 gives detailed information on the variation of the DL with the axial distance.

In Fig. 18, the curve of DL fluctuates in the axial distance from 20 mm to 200 mm, and the change is not obvious, which indicates that the change of the directivity can be ignored. However, as the axial distance increases, the directivity of the sound field still tends to weaken.

4.4 Distribution of sound field of FCACBB

In the above section, we analyzed the distribution characteristics of radiation noise of a FCACBB in the circumferential, radial, and axial directions, respectively. In this section, the characteristics of the whole sound field of bearings radiation noise are discussed as a whole.

According to Fig. 2, the cylindrical coordinate system is transformed into the rectangular coordinate system. The origin of rectangular coordinate system is consistent with that of cylindrical coordinate system. The x-axis coincides with the zero degree position angle and the positive direction is upward, while the z-axis coincides with the bearing axis and the positive direction is outward. The y-axis is perpendicular to the other two coordinate directions, and the coordinate
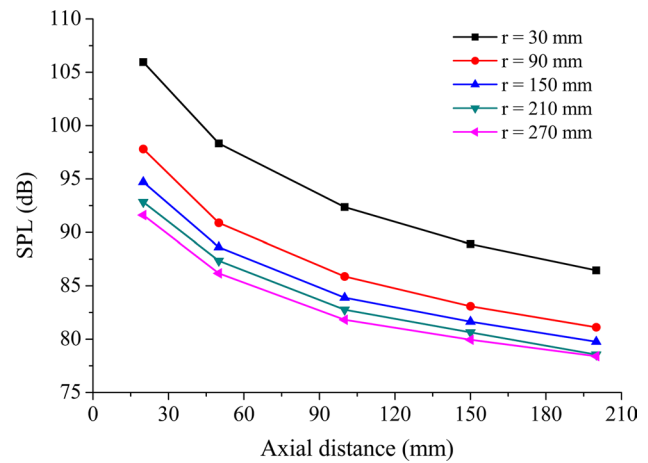
system conforms to the right-hand rule of the Cartesian coordinate system. The coordinate transformation relationship is as follows:

$$
\begin{aligned}
x &= r\cos\theta \\
y &= r\sin\theta \\
z &= l
\end{aligned}
\tag{16}
$$

The whole sound field distribution of radiation noise of a FCACBB in the radial distance from 30 to 270 mm, in the axial distance from 20 to 200 mm, and in the whole circumferential direction is shown in Fig. 19.

It can be seen from Fig. 19, the radiation noise of the FCACBB varies greatly at different field points and the DL of the sound field directivity has significant change in both radial and axial directions. The attenuation of radiation noise
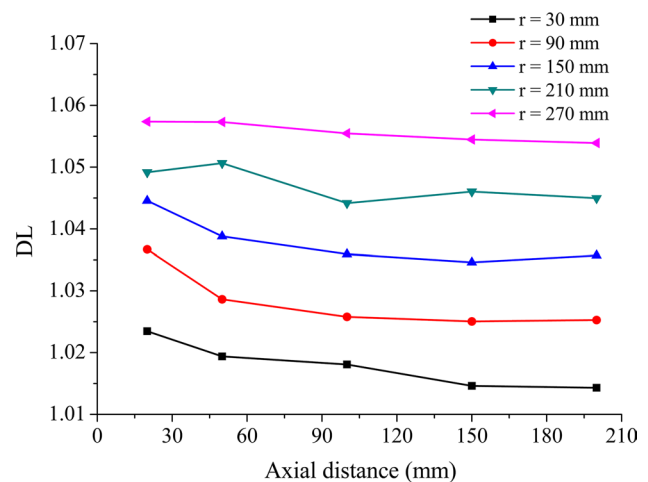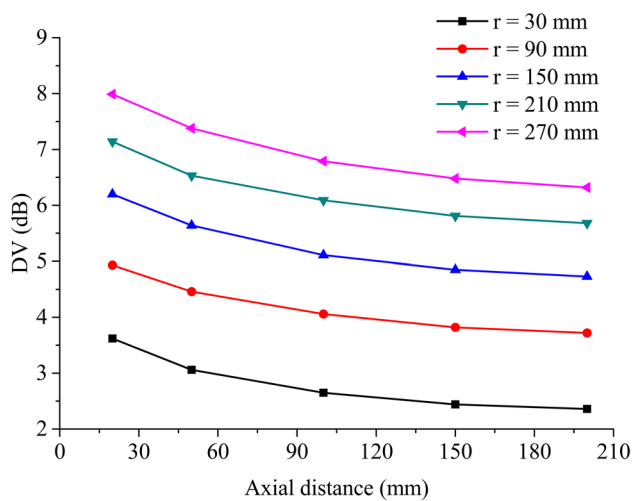

Fig. 21 The DL of radiation noise in the whole circumferential direction

Fig. 22 The DV of radiation noise in the whole circumferential direction

is faster in the axial direction than in the radial direction. The variations are affected by the direction of sound radiation from the interaction of the bearing components. The nonuniform distribution of sound field is due to the strong directivity of radiation noise from the FCACBB.

At a constant speed of 18,000 r min⁻¹, the DA of the sound field is the DA in the friction load zone, which does not change with axial distance and radial distance, and always remains at 225°. This may be the reason that the characteristics of the bearing sound source remain unchanged due to the rotational speed and other operating parameters are constant in the calculation. The SPL_{max}, DL, and DV vary with radial and axial distances as shown in Figs. 20, 21, and 22.

In Fig. 20, the SPL_{max} decreases with the increase in both radial distance and axial distance and attenuates slowly at large radial distance and axial distance, which is related to the propagation of sound with distance. The SPL_{max} in the whole circumferential direction has a variation of 14.34 dB with the radial distance from 30 to 270 mm, and it has a variation of 19.5 dB with the axial distance from 20 to 200 mm. It indicates that the radiation noise of the FCACBB decays much slower in radial direction than in axial direction.

In Fig. 21, when the axial distance is a constant value, the DL tends to increase with the increase in radial distance. It shows that the directivity of the sound field has a clear trend to become obvious with the gradual increase in radial distance from 30 mm to 270 mm. While the radial distance is different constant values, the change of DL is complex and irregular with increasing the axial distance. However, in the whole, the DL slightly weakens in the axial direction. Moreover, when the axial distance is large, the change of DL can be ignored. Therefore, the directivity of the sound field

turns from relatively obvious to less obvious with the axial distance from 20 to 200 mm.

In Fig. 22, the DV increases gradually with the increase in the radial distance and decreases gradually with the increase in the axial distance. When the radial distance is 30 mm, the DV decreases from 3.62 to 2.36 dB with the increase in the axial distance, while the DV decreases from 7.99 to 6.32 dB with the increase in axial distance when radial distance is 270 mm. The directivity of the sound field is opposite to the change trend of the SPL_{max} in the radial direction and similar in the axial direction. The inhomogeneous contacts between the bearing components in the circumferential direction result in different degrees of friction and impact vibration at different locations, which makes DV increase with the increase in radial distance and the decrease in axial distance and makes the radiation noise of the FCACBB have a larger component in the radial direction than in the axial direction. Therefore, from this point of view, it can also be analyzed that the radiation noise attenuates more slowly in the radial direction than in the axial direction, and the circumferential distribution shows more obvious directivity of the sound field with the increase in the radial distance and the decrease in the axial distance.

5 Conclusion

In this paper, the radiation noise model of a FCACBB is established based on the bearing dynamic characteristics and sound radiation theory, and the effectiveness and accuracy of the method are verified by corresponding experiments. Then, the distribution characteristics of the sound field are analyzed in circumferential direction, in radial direction and in axial direction, respectively. Finally, the distribution characteristics of the whole sound field are discussed comprehensively. The results show that the radiation noise increases with the increase in the rotational speed, and the directivity of the sound field intensifies simultaneously. Meanwhile, the DA of the sound field moves upward along with the rotation direction from low position at the right lower semicircle. The variation trend of the radiation noise in the friction load zone is similar to that in the impact load zone, and the SPL of the former is large and dominant. The radiation noise attenuates gradually with the increase in the distance, and yet the DA of the sound field remains unchanged. However, the radiation noise has a larger component in the radial direction than in the axial direction and the directivity of the sound field has different changes in the both directions. It becomes more obvious with the increase in the radial distance, but diminishing weakens with the increase in the axial distance. The results reveal a distribution law of the sound field of the FCACBBs in circumferential, radial, and axial

directions. The conclusions can provide a reference for further optimizing the sound field of FCACBBs.

Compliance with ethical standards

Conflict of interest The authors declare that they have no conflict of interest.

References

1. Cerrada M, Sánchez R, Li C, Pacheco F, Cabrera D, Oliveira JV, Vásquez RE (2018) A review on data-driven fault severity assessment in rolling bearings. Mech Syst Signal Pr 99:169–196
2. Xia H, Qiao G, Zhou S, Wang J (2013) Reciprocating friction and wear behavior of reaction-formed SiC ceramic against bearing steel ball. Wear 303(1–2):276–285
3. Yin Z, Yuan J, Huang C, Wang Z, Huang L, Cheng Y (2016) Friction and wear behaviors of Al_2O_3/TiC micro-nano-composite ceramic sliding against metals and hard materials. Ceram Int 42(1):1982–1989
4. Cao H, Niu L, Xi S, Chen X (2018) Mechanical model development of rolling bearing-rotor systems: a review. Mech Syst Signal Pr 102:37–58
5. Bai C, Zhang H, Xu Q (2008) Effects of axial preload of ball bearing on the nonlinear dynamic characteristics of a rotor-bearing system. Nonlinear Dyn 53(3):173–190
6. Bizarre L, Nonato F, Cavalca KL (2018) Formulation of five degrees of freedom ball bearing model accounting for the nonlinear stiffness and damping of elastohydrodynamic point contacts. Mech Mach Theory 124:179–196
7. Zhang X, Han Q, Peng Z, Chu F (2015) A new nonlinear dynamic model of the rotor-rearing system considering preload and varying contact angle of the bearing. Commun Nonlinear Sci 22(1–3):821–841
8. Wang Y, Wang W, Zhang S, Zhao Z (2018) Effects of raceway surface roughness in an angular contact ball bearing. Mech Mach Theory 121:198–212
9. Harsha SP, Sandeep K, Prakash R (2004) Nonlinear dynamic response of a rotor bearing system due to surface waviness. Nonlinear Dyn 37(2):91–114
10. Liao TN, Lin JF (2002) Ball bearing skidding under radial and axial loads. Mech Mach Theory 37(1):91–113
11. Han Q, Chu F (2015) Nonlinear dynamic model for skidding behavior of angular contact ball bearings. J Sound Vib 354:219–235
12. Zhang W, Deng S, Chen G, Cui Y (2017) Impact of lubricant traction coefficient on cage's dynamic characteristics in high-speed angular contact ball bearing. Chin J Aeronaut 30(2):827–835
13. Jiang S, Mao H (2010) Investigation of variable optimum preload for a machine tool spindle. Int J Mach Tool Manu 50(1):19–28
14. Jiang S, Zheng S (2010) A modeling approach for analysis and improvement of spindle-drawbar-bearing assembly dynamics. Int J Mach Tool Manuf 50(1):131–142
15. Jiang S, Zheng S (2010) Dynamic design of a high-speed motorized spindle-bearing system. J Mech Des 132(3):034501-1–034501-5
16. Zhang Y, Li X, Hong J, Yan K, Li S (2018) Uneven heat generation and thermal performance of spindle bearings. Tribol Int 126:324–335
17. Yan K, Wang Y, Zhu Y, Hong J, Zhai Q (2016) Investigation on heat dissipation characteristic of ball bearing cage and inside cavity at ultra high rotation speed. Tribol Int 93:470–481
18. Than V-T, Huang JH (2016) Nonlinear thermal effects on high-speed spindle bearings subjected to preload. Tribol Int 96:361–372
19. Zheng D, Chen W (2017) Thermal performances on angular contact ball bearing of high-speed spindle considering structural constraints under oil-air lubrication. Tribol Int 109:593–601
20. Zheng D, Chen W, Li M (2018) An optimized thermal network model to estimate thermal performances on a pair of angular contact ball bearings under oil-air lubrication. Appl Therm Eng 131:328–339
21. Khanam S, Dutt JK, Tandon N (2015) Impact force based model for bearing local fault identification. J Vib Acoust 137(5):051002-1–051002-13
22. Wang W, Zhang S, Zhao Z, Ai S (2015) Effect of the inhomogeneity in races on the dynamic behavior of rolling bearing. J Vib Acoust 137(6):061015-1–061015-19
23. Patil MS, Mathew J, Rajendrakumar PK, Desai S (2010) A theoretical model to predict the effect of localized defect on vibrations associated with ball bearing. Int J Mech Sci 52(9):1193–1201
24. Zhang J, Lu X, Lin J, Ma L, Wang J (2017) Dynamic analysis of a rotor-bearing-SFD system with the bearing inner race defect. Shock Vib Article ID 2489376
25. Rho B-H, Kim K-W (2003) Acoustical properties of hydrodynamic journal bearings. Tribol Int 36(1):61–66
26. Bouaziz S, Fakhfakh T, Haddar M (2012) Acoustic analysis of hydrodynamic and elasto-hydrodynamic oil lubricated journal bearings. J Hydrodyn Ser B 24(2):250–256
27. Li S, Wu Y, Zhang K (2010) Parameter optimization for oil/air lubrication of high speed ceramic motorized spindle without bearing inner rings. Appl Mech Mater 37–38:839–843
28. Danzer R (2014) On the relationship between ceramic strength and the requirements for mechanical design. J Eur Ceram Soc 34(15):3435–3460
29. Jiang S, Mao H (2011) Investigation of the high speed rolling bearing temperature rise with oil-air lubrication. J Tribol 133(2):021101-1–021101-9
30. Mo J, Wang Z, Chen G, Shao T, Zhu M, Zhou Z (2013) The effect of groove-textured surface on friction and wear and friction-induced vibration and noise. Wear 301(1–2):671–681
31. Wang A, Mo J, Wang X, Zhu M, Zhou Z (2018) Effect of surface roughness on friction-induced noise: exploring the generation of squeal at sliding friction interface. Wear 402–403:80–90
32. Ouenzerfi G, Massi F, Renault E, Berthier Y (2015) Squeaking friction phenomena in ceramic hip endoprosthesis: modeling and experimental validation. Mech. Syst. Signal Pr. 58–59:87–100
33. Deng S, Jia Q, Xue J (2014) Design principle of rolling bearings. China Standard Press, Beijing **(Chinese)**
34. Fang B, Zhang J, Wan S, Hong J (2018) Determination of optimum preload considering the skidding and thermal characteristic of high-speed angular contact ball bearing. J Mech Des 140:053301-1–053301-11
35. Cao Y, Altintas Y (2004) A general method for the modeling of spindle-bearing systems. J Mech Des 126:1089–1104
36. Wang Y, Wang W, Zhang S, Zhao Z (2015) Investigation of skidding in angular contact ball bearings under high speed. Tribol Int 92:404–417
37. Li S, Huang Q (2010) An improved form of the hypersingular boundary integral equation for exterior acoustic problems. Eng Anal Bound Elem 34(3):189–195

38. Sarıgül AS, Seçgin A (2004) A study on the applications of the acoustic design sensitivity analysis of vibrating bodies. Appl Acoust 65(11):1037–1056

39. Li Y, Mulani SB, Fei Q, Wu S, Zhang P (2017) Vibro-acoustic analysis under stationary and non-stationary random excitations with KLE/FEM/BEM. Aerosp Sci Technol 66:203–215

40. Wang Z, Zhao Z, Liu Z, Huang Q (2009) A method for multi-frequency calculation of boundary integral equation in acoustics based on series expansion. Appl Acoust 70(3):459–468